Image analysis techniques for automated IVUS contour detection

Maria Papadogiorgaki, Vasileios Mezaris, Yiannis S. Chatzizisis, George D. Giannoglou and Ioannis Kompatsiaris

Abstract—**Intravascular ultrasound (IVUS) constitutes a valuable technique for the diagnosis of coronary atherosclerosis. The detection of lumen and media-adventitia borders in IVUS images represents a necessary step towards the reliable quantitative assessment of atherosclerosis. In this work a fully automated technique for the detection of lumen and media-adventitia borders in IVUS images is presented. This comprises two different steps for contour initialization, one for each corresponding contour of interest, and a procedure for the refinement of the detected contours. Intensity information, as well as the result of texture analysis, generated by means of a multilevel Discrete Wavelet Frames decomposition, are used in two different techniques for contour initialization. For subsequently producing smooth contours, three techniques based on low-pass filtering and Radial Basis Functions are introduced. The different combinations of the proposed methods are experimentally evaluated in large datasets of IVUS images derived from human coronary arteries. It is demonstrated that our proposed segmentation approaches can quickly and reliably perform automated segmentation of IVUS images.**

Index Terms—**Intravascular ultrasound, Contour detection, Segmentation, Radial Basis Functions**
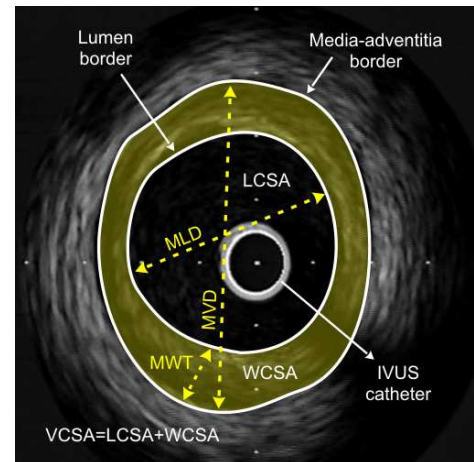
Fig. 1. A typical IVUS image with the lumen and media-adventitia borders demarcated (LCSA, lumen cross-sectional area, VCSA, vessel cross-sectional area, WCSA, wall cross-sectional area). (Reprinted from Giannoglou et al. (2007))

I. INTRODUCTION AND LITERATURE

Medical images derived from several technologies (e.g., X-ray, ultrasound, computed tomography, magnetic resonance, nuclear imaging) are extensively used to improve the existing diagnostic systems and facilitate medical research. Coronary angiography is acknowledged as the gold standard for the diagnosis of coronary artery disease. However, coronary angiography is restricted by its inherent inability to depict the arterial wall, since it illustrates only the silhouette of the coronary lumen. In the last two decades, intravascular ultrasound (IVUS) has been introduced as a complementary to angiography diagnostic technique aiming to provide more accurate imaging of coronary atherosclerosis (Mintz et al., 2001).

IVUS is a catheter-based technique that renders two-dimensional cross-sectional images of the coronary arteries, and provides information concerning the lumen and wall. In a typical IVUS image three arterial regions can be distinguished: the lumen, the vessel wall, consisting of the intima and the media layers, and the adventitia plus surroundings (Fig. 1). The above regions are separated by two borders: the lumen border,

which corresponds to the lumen-wall interface, and the media-adventitia border, which represents the boundary between the media and adventitia (Mintz et al., 2001). The reliable and quick detection of these two borders is the goal of IVUS image segmentation and also the basic step towards the geometrically correct 3D reconstruction of the arteries (Giannoglou et al., 2006a), (Slager et al., 2000), (Coskun et al., 2003).

Traditionally, the segmentation of IVUS images has been performed manually, which is a time-consuming procedure affected by high inter- and intra-user variability. To overcome these limitations, several approaches for semi-automated segmentation have been proposed. In (Herrington et al., 1992) after manual indication of the general location of the boundary of interest by the user, an edge detection filter is applied to find potential edge points within the pointed neighborhood. The extracted image data are used for the estimation of the closed smooth final contour. Sonka et al. (Sonka et al., 1995) implemented a knowledge-based graph searching method incorporating a priori knowledge on coronary artery anatomy and a selected region of interest prior to the automated border detection.

Quite a few variations of active contour model have been investigated (Kompatsiaris et al., 2000), (Chatzizisis, 2004) including the approach of (Parissi et al., 2006). There, user interaction is required for the drawing of an initial contour as close as possible to its final position; using this initial contour, the active contour approximates the final desired

M. Papadogiorgaki, Vasileios Mezaris and I. Kompatsiaris are with the Informatics and Telematics Institute (ITI) / Centre for Research and Technology Hellas (CERTH), Thessaloniki 57001, Greece. Y.S. Chatzizisis and G.D. Giannoglou are with the Cardiovascular Engineering and Atherosclerosis Laboratory, AHEPA University Hospital, Aristotle University Medical School, GR-54636, Thessaloniki, Greece.

border. The active contour or deformable model principles have also been used for the extraction of the lumen and medial-adventitia borders in three dimensions after setting an initial contour (Kovalski et al., 2000), (Klingensmith et al., 2000). However, in this approach the contour detection fails for low contrast interface regions such as the lumen border, which in most images corresponds to weak pixel intensity variation. In order to improve the active surface segmentation algorithm for plaque characterization, Klingensmith et al. (Klingensmith et al., 2004) used the frequency information after acquiring the radio-frequency (RF) IVUS data. RF data were also used in (Perrey et al., 2004) after in vivo acquisition for the segmentation of the lumen boundary in IVUS images. According to this approach, tissue describing parameters were directly estimated from RF data and a neuro-fuzzy inference system was used to distinguish blood from tissue regions. Cardinal et al. (Cardinal et al., 2006) presented a 3D IVUS segmentation applying Rayleigh probability density functions (PDFs) for modelling the pixel grey value distribution of the vessel wall structures, requiring, however, some manual tracing of contours for initialization.

Despite facilitating the analysis of IVUS data as compared to their completely manual processing, the aforementioned methods pose the restriction of needing substantial human intervention during the analysis process. This has proven quite restrictive for clinical practice, where fully automated approaches would be most attractive. A limited number of approaches focusing on the minimization of human intervention has been developed so far, such as the segmentation based on edge contrast (Zhu et al., 2002); the latter was shown to be an efficient feature for IVUS image analysis, in combination with the grey level distribution. Specific automated approaches which utilize the deformable model principles in combination with other various techniques and features reported in the related literature have also been investigated. Brusseau et al. (Brusseau et al., 2004) exploited an automated method for detecting the endoluminal border based on an active contour. This evolves until it optimally separates regions with different statistical properties without using a pre-selected region of interest or initialization of the contour close to its final position. However, in (Brusseau et al., 2004) the detection of the media-adventitia boundary was not examined. Similarly, (dos S. Filho et al., 2005) employed a fuzzy clustering technique for the detection of the lumen boundary alone. Another approach based on deformable models was reported by Plissiti et al. (Plissiti et al., 2004), who employed a Hopfield neural network for the modification and minimization of an energy function, as well as a priori vessel geometry knowledge. Despite being to a significant extent automated, this method still requires manual estimation of the boundaries in the first frame of the sequence of IVUS images. Unal et al. proposed in (Unal et al., 2006) a shape-driven approach to the segmentation of IVUS images, based on building a shape space using training data and consequently constraining the lumen and media-adventitia contours to a smooth, closed geometry in this space. An automated approach for segmentation of IVUS images based on a variation of an active contour model was presented in (Giannoglou et al., 2007). The technique was in

vivo evaluated in images originating from human coronary arteries. The initialization of the contours in each IVUS frame was automatically performed using an algorithm based on the intensity features of the image. The initially extracted boundaries constituted the input to the active contour model, which then deformed the contours appropriately, identifying their correct location on the IVUS frame; however, contour initialization based on intensity information alone is not most efficient, as discussed in the Results section below.

Other approaches reported in the literature for the computer-assisted interpretation of IVUS images were based on the calculation of the image energy for contour detection, or on the detection of calcification regions, which could in turn be used for contour detection. A technique for the automated detection of calcification regions based on fuzzy clustering was proposed in (dos S. Filho et al., 2004); however, it remains unclear how this should be used for assisting the automated detection of the lumen and media-adventitia boundaries. In (Luo et al., 2003) the lumen area only of the coronary artery was estimated using an internal energy, which describes the smoothness of the arterial wall, and an external energy, which represents the grayscale variation of the images that constitute the IVUS sequence; the minimal energy that defines the contour was obtained using circular dynamic programming. As opposed to (Luo et al., 2003), the media-adventitial boundary only was considered in (Gil et al., 2006), where statistical classification techniques were used for modelling the adventitia region.

This paper presents a novel method for the fully automated detection of lumen and media-adventitia boundaries in IVUS images. Intensity information, as in (Giannoglou et al., 2007), as well as the result of texture analysis, generated by means of a multilevel Discrete Wavelet Frames decomposition, is used in two different techniques for the initialization of the lumen and media-adventitia contours. For the subsequent smoothing of these initial contours, three techniques based on low-pass filtering and Radial Basis Functions (RBFs) are introduced. The different combinations of the proposed methods are experimentally evaluated. Evaluation results show that the combination of texture-based initialization and RBF-based smoothing outperforms the other combinations and succeeds in automatically generating results that are in good agreement with those of manual segmentation.

II. MATERIALS AND METHODS

A. Preprocessing and Feature Extraction

1) Preprocessing: As outlined above, the proposed method uses intensity and texture features for contour initialization. Preprocessing of the image data for the purpose of contour detection and in particular for the application of a texture description method to the data consists of two steps: (a) representation of the images in polar coordinates, and (b) removal of catheter-induced artifacts.

Representation of the images in polar coordinates is important for facilitating the description of local image regions in terms of their radial and tangential characteristics. It also facilitates a number of other detection steps, such as contour initialization and the smoothing of the obtained contour. For
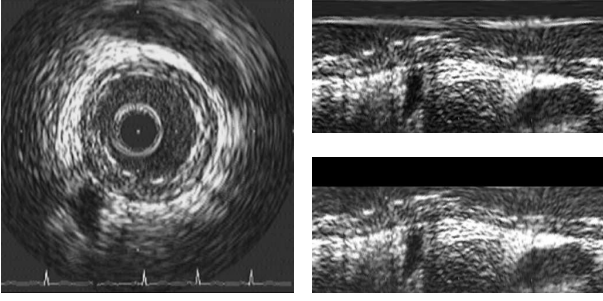
Fig. 2. Original IVUS image (left) and corresponding polar coordinate images before (right top) and after (right bottom) the removal of catheter-induced artifacts.

this purpose, each of the original IVUS images is transformed to a polar coordinate image where columns and rows correspond to angle and distance from the center of the catheter, respectively, and this image alone, denoted $I(r,\theta)$, is used throughout the analysis process.

The IVUS images include not only tissue and blood regions, but also the outer boundary of the catheter itself. The latter defines a dead zone of radius equal to that of the catheter, where no useful information is contained. Knowing the diameter D of the catheter, these catheter-induced artifacts are easily removed by setting $I(r,\theta) = 0$ for $r < D/2+e$, e being a small constant. This preprocessing is illustrated in Fig. 2.

2) Texture analysis: Texture has been shown to be an important cue for the analysis of generic images (Mezaris et al., 2004). In this work, the Discrete Wavelet Frames (DWF) decomposition (Unser, 1995) is used for detecting and characterizing texture properties in the neighborhood of each pixel. This is a method similar to the Discrete Wavelet Transform (DWT) that uses a filter bank to decompose the grayscale image to a set of subbands. The main difference between DWT and DWF is that in the latter the output of the filter bank is not subsampled. The DWF approach has been shown to decrease the variability of the estimated texture features, thus improving pixel classification for the purpose of image segmentation. The employed filter bank is based on the lowpass Haar filter

$$H(z) = \frac{1}{2}(1 + z^{-1}) \tag{1}$$

Using this along with the complementary highpass filter $G(z)$, defined as $G(z) = zH(-z^{-1})$, the fast iterative scheme proposed in (Unser, 1995) for applying the DWF analysis in the two-dimensional space is realized. Then, according to the DWF theory, the texture of pixel p can be characterized by the standard deviations of all detail components, calculated in a neighborhood F of pixel p. The calculation of these standard deviations is denoted by the σ blocks in Fig. 3. The images resulting from treating each calculated standard deviation as intensity value of pixel p are denoted as I_k, $k = 1, \ldots, K$. In the proposed approach, a DWF decomposition of four levels is employed, resulting in $K = 12$ such images, in addition to an approximation component, which is a low-pass filtered image denoted I_{LL}. However, not all of these images are used for

the localization of the contours, as discussed in the Contour Initialization section below.

B. Contour Initialization

The objective of the contour initialization procedure is the detection of pixels that are likely to belong to the lumen and media-adventitia boundaries, taking into consideration the previously extracted texture features. Two approaches for the initialization of the lumen contour are considered in this work; they mainly differ in the features that they rely on for the initialization: intensity features and texture features, respectively.

1) Lumen contour initialization using intensity information: The use of intensity information readily available from the IVUS image $I(r,\theta)$ after the preprocessing stage is a common approach to contour initialization, since intensity is the simplest form of information that can be used for detecting the lumen boundary. The lumen boundary, when travelling from the center of the catheter towards the image borders on a radius R (i.e. for $\theta = const$) is typically denoted by an increase of intensity from $I(r,\theta) < e'$, e' being a small constant, to $I(r,\theta) \gg e'$ (e.g. Fig. 2); assuming the presence of no artifacts (noise) in the lumen area, inequality $I(r,\theta) < e'$ should hold for all pixels belonging to the lumen area.

Consequently, the lumen contour can be initialized as the set of pixels (Giannoglou et al., 2007):

$$c_{int,i} = \{\mathbf{p}_{int,i} = [\rho, \theta]\} \tag{2}$$

for which

$$I(\rho, \theta) > T \quad \text{and} \quad I(r, \theta) < T \ \forall r < \rho \tag{3}$$

where subscript int in Eq. 2 denotes the Lumen (i.e. "internal") contour, subscript i denotes intensity-based initialization and T is a threshold. This initialization defines a lumen contour function $C_{int,i}(\theta) = \rho$ (Fig. 4(a)).

2) Lumen contour initialization using texture information: Intensity information can be used, as described above, for the initialization of the lumen boundary. However, it can be argued that there is more information in an IVUS image than just an intensity increase on the lumen-wall boundary that can be used for differentiating between the lumen and wall areas (Papadogiorgaki et al., 2006). More specifically, these two areas demonstrate different texture characteristics: the lumen area tends to be a low-intensity non-textured region, with noise being responsible for any high-intensity artifacts in it, whereas the wall area is typically characterized by the presence of both low-intensity and high-intensity parts, with changes between the two that are of relatively low-frequency in the tangential direction and of somewhat higher frequency in the radial direction. Consequently, the local energy of the signal in appropriate frequency sub-bands can be used as a criterion for differentiating between the lumen and wall areas; to this end, the results of texture analysis previously discussed are employed.

More specifically, let $I_{int,t}$ denote the "image" that is used for the detection of the lumen boundary in the case of texture-based initialization. This is defined using the results of texture
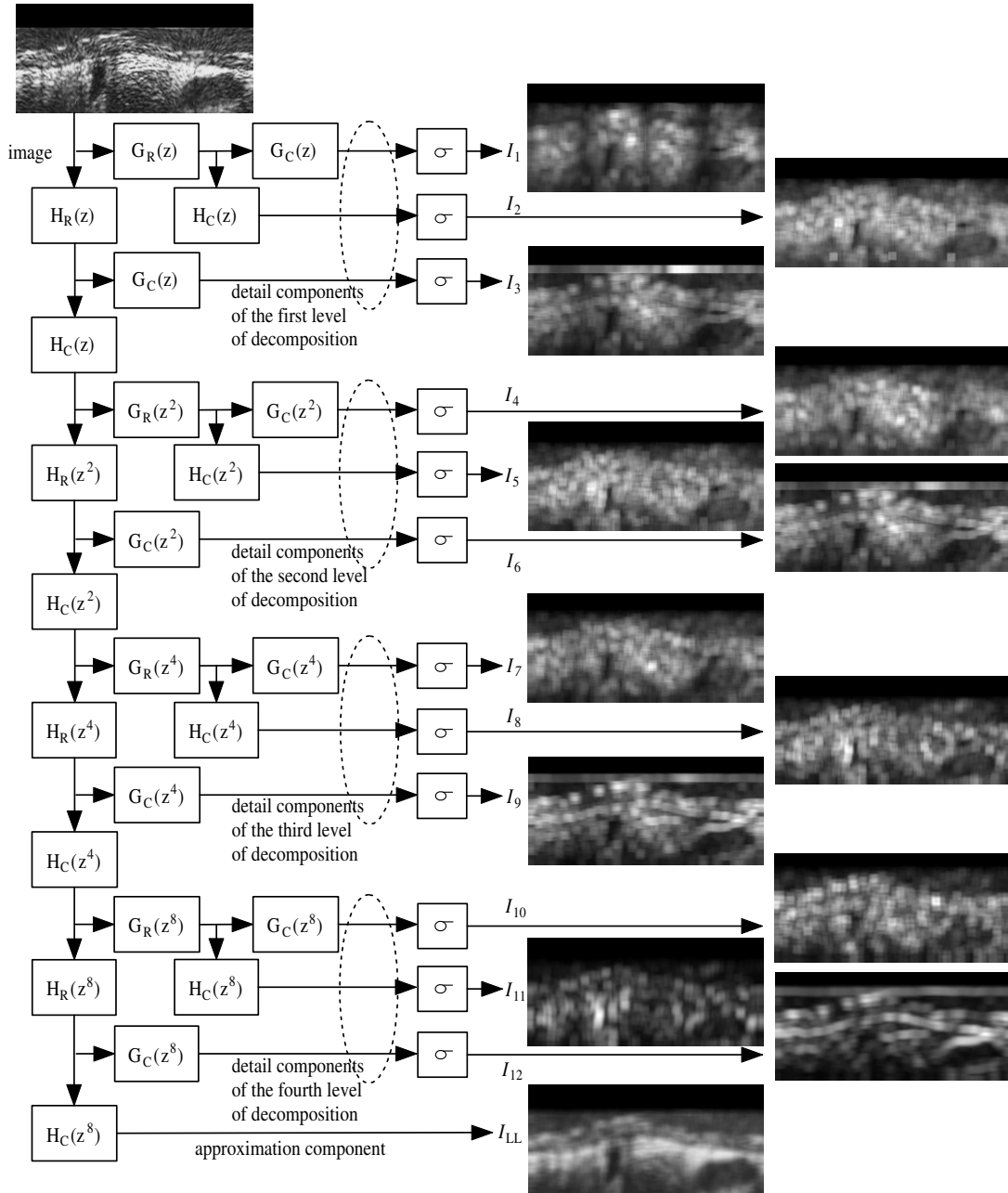
Fig. 3.   Fast iterative 2D DWF decomposition of four levels. Subscripts R, C denote filters applied row-wise and column-wise, respectively.

analysis as

$$I_{int}(r,\theta) = \frac{255}{\max_{(r,\theta)}\{I'_{int}(r,\theta)\}} I'_{int}(r,\theta) \qquad (4)$$

$$I'_{int}(r,\theta) = \sum_{k=\{7,8,10,11\}} I_k(r,\theta) \qquad (5)$$

An example image generated using Eq. 4 can be seen in Fig. 4(b). The choice of the images I_k (Fig. 3) that are employed in this initialization process was done based on visual evaluation of all K generated images and is in line with the aforementioned observations regarding the texture properties of the lumen and wall areas, in combination with

the characteristics of the filter bank used for the generation of images I_k .

Using the above image data, the lumen contour is initialized as the set of pixels

$$c_{int,t} = \{\mathbf{p}_{int,t} = [\rho,\theta]\} \qquad (6)$$

for which

$$I_{int,t}(\rho,\theta) > T \quad \text{and} \quad I_{int,t}(r,\theta) < T \; \forall r < \rho \qquad (7)$$

thus defining a lumen contour function $C_{int,t}(\theta) = \rho$ (Fig. 4(b)). T is the threshold already defined for intensity-based initialization.
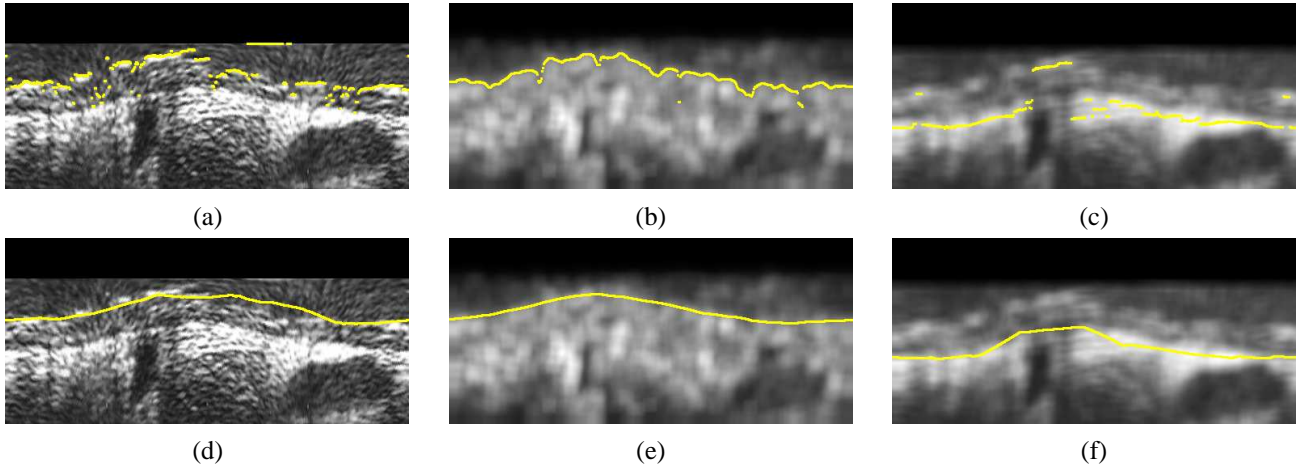
Fig. 4. Results of contour initialization for (a) the lumen, using intensity information, (b) the lumen, using texture information, (c) the media-adventitia boundary, and (d), (e), (f) the corresponding contours after contour refinement using LPF-based approximation.

3) Media-adventitia contour initialization: The motivation behind the choice of image data to be used for the initialization of the media-adventitia boundary lies under the proposed approach in the observation that in many cases the adventitia is represented in IVUS images by a thick bright ring (a thick bright zone in polar coordinates) that is dominant in the image, as opposed to the media region or any other region of an IVUS image. Consequently, for the localization of the adventitia region, low-pass filtering could be used to suppress undesirable details of the image while preserving well the former.

Based on the above observation, the detail component I_{LL} of the DWF decomposition discussed in the Texture Analysis section is used in this work for detecting the media-adventitia boundary. Using this, the media-adventitia contour is initialized as the set of pixels

$$c_{ext} = \{\mathbf{p}_{ext} = [\mu, \theta]\} \tag{8}$$

for which

$$I_{LL}(\mu, \theta) = \max_{r > \rho}\{I_{LL}(r, \theta)\}, \tag{9}$$

where $[\rho, \theta]$ are the points of the lumen contour, as obtained by the initialization process. This defines a contour function $C_{ext}(\theta) = \mu$ for the media-adventitia contour (Fig. 4(c)).

Selecting, according to the above equations, the pixels to which the intensity of the low-pass filtered image is maximized serves the purpose of identifying the most dominant low-frequency detail in the image, in case low-pass filtering has failed to suppress all other higher-frequency information. The selected pixels correspond to those on the boundary between the adventitia and the media regions.

C. Contour Refinement

In contrast to the initial contours generated as described in the previous section, which are not smooth and are characterized by discontinuities (Fig. 4(a), (b) and (c)), the true lumen and media-adventitia boundaries are smooth, continuous functions of θ. Consequently, in order to obtain smooth contours that are consistent with the true ones, the application of a filtering or approximation procedure to the initial contour
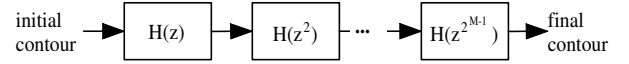

Fig. 5. Illustration of the low-pass filtering-based contour smoothing procedure.

functions $C_{int}(\theta)$, $C_{ext}(\theta)$ is required. In this work, two different approaches are used: one based on low-pass filtering (LPF) of the non-smooth, non-continuous contour functions generated by the initialization process, and one based on Radial Basis Function (RBF) approximation.

1) LPF-based contour smoothing: LPF-based contour smoothing is a common approach, realized in this work by applying a simple filtering solution that takes advantage of the filtering functionalities developed for the purpose of texture analysis. More specifically, the low-pass filters $H(z^{2^i})$, $i = 0, \ldots, M - 1$ that are based on the low pass Haar filter (Eq. 1) are successively applied to each of the two initial contour functions (Fig. 5). Parameter M controls the smoothness of the resulting contour and was set to 7 for the purpose of this application, based on experimentation. Results of this process are illustrated in Fig. 4(d), (e) and (f). This simple procedure is shown to perform acceptably in smoothing the contours; however, better results can be obtained using a more elaborate approximation technique such as one based on radial basis functions, as discussed in the following section and also shown in the Results section.

2) RBF-based contour approximation: Polyharmonic Radial Basis Functions (Carr et al., 2001) have been proposed for reconstructing smooth surfaces from point-cloud data and for repairing incomplete meshes through interpolation methods and approximation techniques. Under this approach, the desired smooth surface is defined as the zero set of an RBF s fitted to the given initial surface data, i.e. as the set of points x for which $s(x) = 0$. An RBF s is defined as a function of

the following form

$$s(x) = p(x) + \sum_{i=1}^{N} \lambda_i \phi(|x - x_i|), \qquad (10)$$

where x is a point in the 2-dimensional (2D) or 3-dimensional (3D) space, depending on whether the curve to be approximated is a 2D curve or a 3D surface, where the RBF s is evaluated; $p(x)$ is a low degree polynomial, ϕ is a real function called basic function, x_i are the centers of the RBF, λ_i are the RBF coefficients, and $|.|$ denotes here Euclidean distance measured in the polar coordinate image. Fitting an RBF to the given initial data refers to calculating the RBF coefficients λ_i and the weights of $p(x)$.

Various functions have been proposed for serving as a basic function ϕ (Carr et al., 2001). In this work, the biharmonic spline was used:

$$\phi(|x - x_i|) = |x - x_i|^2 \ln(|x - x_i|) \qquad (11)$$

The centers x_i appearing in Eqs. 10 and 11 above are a subset of the points in the 2D or 3D space at which a function f has been defined. The latter represents the initial input data that the RBF is to approximate and is defined as discussed separately for the 2D and 3D cases in the two following subsections.

3) RBF-based contour approximation in the 2D space: The use of an RBF for the approximation of one of the initial contours in a frame, i.e. the generation of a contour c' that is a smooth, reasonable approximation of c, requires the definition for each such contour of a function f, as follows:

$$f(\theta, C(\theta)) = 0 \qquad (12)$$

where $C(\theta)$ here denotes either $C_{int}(\theta)$ or $C_{ext}(\theta)$, depending on the contour being examined. Function f is used for formulating the approximation problem as one of finding an RBF s for which $s(.) \simeq f(.)$. To avoid the trivial solution of s being zero at every point, f must also be defined for a set of points not belonging to the initial contour (off-surface points), so that

$$f(\theta, r \neq C(\theta)) \neq 0 \qquad (13)$$

In order to avoid identifying as off-surface points at this stage points which potentially belong to the true contour under examination, the former points are defined in this work as those which satisfy the following equations:

$$r = \max_{\theta}\{C(\theta)\} + 1 \qquad (14)$$

$$r = \min_{\theta}\{C(\theta)\} - 1 \qquad (15)$$

For the above points in the 2D space, function f is defined as the signed Euclidean distance from the initialized contour for $\theta = const$, i.e.

$$f(\theta, r \neq C(\theta)) = r - C(\theta) \qquad (16)$$

Following the definition of f, the FastRBF library (FarField, 2001) is used to generate the smooth contour approximation c', as follows: First, duplicate points where f has been defined (i.e. points in the 2D space which are located within a specific

minimum distance from other input points) are removed; the remaining points serve as the centers of the RBF, x_i, that were defined in the previous section. Subsequently, the fitting of an RBF to this data is performed using the spline smoothing technique, chosen for not requiring the prior estimation of the noise measure related to each input data point, as opposed to other fitting options such error bar fitting. Finally the fitted RBF is evaluated in order to find the points which correspond to zero value; the latter define the contour approximation c'. An illustrative example of the final smooth curve generated using the results of initialization and the off-surface points selected according to the above procedure is shown in Fig. 6.

4) RBF-based contour approximation in the 3D space: Under the approach described in the previous section, the RBF-based approximation was applied to each frame independently. However, a similar process can be applied to all frames, so as to directly generate a smooth surface in the 3D space for each of the two boundaries of interest (i.e. lumen and media-adventitia). In the absence of any information regarding the correct spatial localization of each 2D plane (represented by a frame of the IVUS image sequence) in the 3D space, each point $[C_t(\theta), \theta]$ belonging to the examined boundary at frame t ($t \in [0, L-1]$) according to the initialization procedure (whichever is employed) is represented in the 3D space as $[C_t(\theta), \theta, t]$ (the index t is introduced to $C(\theta)$ here simply to differentiate between initial contour functions at different frames of the image sequence).

Similarly to the 2D case, function f is defined as follows:

$$f(\theta, C_t(\theta), t) = 0 \qquad (17)$$

and

$$f(\theta, r \neq C_t(\theta), t) = r - C_t(\theta) \qquad (18)$$

for the points $[\theta, r, t]$ that satisfy the following equations:

$$r = \max_{\theta,t}\{C_t(\theta)\} + 1 \qquad (19)$$

$$r = \min_{\theta,t}\{C_t(\theta)\} - 1 \qquad (20)$$

Similarly with the 2D case, the FastRBF library was then used, to generate in this case the smooth 3D contour approximation over the whole sequence of IVUS frames.

D. In-vivo validation of segmentation techniques

1) IVUS image datasets: To validate in-vivo the proposed segmentation techniques, we investigated with IVUS 18 arterial segments (right coronary artery, RCA, $n = 7$; left anterior descending, LAD, $n = 5$; left circumflex artery, LCx $n = 6$) from 10 patients randomly selected during routine diagnostic and therapeutic interventional procedures. From this pool of IVUS images we selected a dataset of (a) 270 IVUS images (i.e. 30 consecutive gated images per artery from 8 arteries, and 30 randomly selected images from the remaining 9 arteries) acquired with a mechanical IVUS imaging system (ClearView, Boston Scientific, Natick, MA, USA) using a 2.6F, 40 MHz IVUS catheter (Atlantis SR Pro, Boston Scientific, Natick, MA, USA), and (b) 50 IVUS images, all from the same arterial segment, acquired with a solid-state electronic
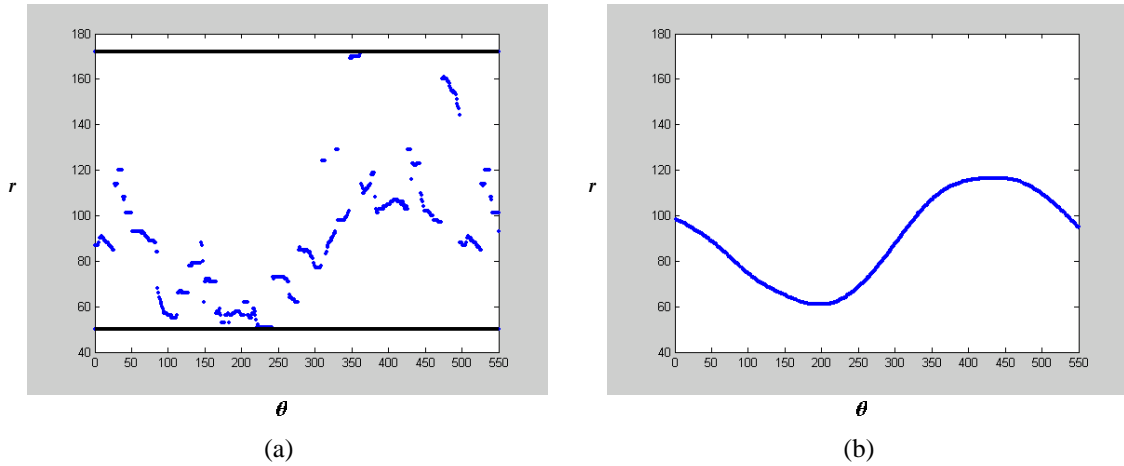
Fig. 6. Example of 2D RBF-based contour smoothing in polar representation: (a) contour initialization results (in blue) and selected off-surface points (in black), (b) final smooth contour generated by 2D RBF-based contour smoothing.

IVUS imaging system (Volcano Therapeutics Inc. Rancho Cordova, CA, USA) using a 2.9F, 20 MHz IVUS catheter. In the mechanical imaging system a motorized pullback device was used to withdraw the IVUS catheters at a constant speed of 0.5 mm/sec. The ultrasound data was recorded in a 0.5-inch S-VHS videotape. The S-VHS data was digitized at 512×512 pixels with 8-bit grey scale in a rate of 7.5 images/sec and the end-diastolic images were selected (peak of R-wave on ECG) (Giannoglou et al., 2006a). In the solid-state imaging system the ultrasound data were digitally recorded in DICOM along with the ECG, which was used for the selection of end-diastolic images (peak of R-wave on ECG). The Institutional Medical Ethics Committee approved the study, and all patients gave written informed consent.

2) Method comparison study: Each of these images was segmented manually by an experienced expert, and automatically with each of the six possible combinations of the two lumen contour initialization approaches (intensity-based and texture-based) and the three contour refinement approaches (LPF, 2D RBF and 3D RBF-based) presented in the Materials and Methods section. The inter-observer and intra-observer agreement of manual segmentation was previously tested and found to be extremely high (Giannoglou et al., 2007).

For this comparison three morphometric parameters were calculated in each IVUS image: these were the Lumen cross-sectional area-LCSA, Vessel cross-sectional area-VCSA, and Wall area-cross-sectional WCSA, (Fig. 1). The values of these parameters in the manually segmented images were used as reference.

For the temporal evaluation of the automated segmentation versus the manual reference, the mean duration per frame of manual and automated segmentation were also calculated and compared.

3) Statistical analysis: The statistical analysis of the results expressed by the parameters was performed with the statistical package SPSS 12.0 (SPSS Inc, Chicago, IL, USA). For the method comparison study, Bland-Altman analysis, and linear regression analysis were applied. $P < 0.05$ was considered as the level of significance.

III. RESULTS

A. Results of automated versus manual segmentation

The differences between automated and manual tracings, for the images acquired with the mechanical IVUS system "Boston Scientific", are presented in Figs. 7 to 9 (Bland-Altman and linear regression plots) and Table I (Md±SD, i.e. mean and standard deviation of the differences between automated and manual tracings). These results reveal the improved overall performance of the approach that uses texture features for lumen boundary initialization and 2D RBFs for contour approximation, as compared to the other combinations of initialization and contour smoothing techniques considered in this work. Also, in this approach, as depicted in the corresponding plots, the vast majority of differences were distributed within the limits of agreement (i.e. Md±2SD), suggesting a high level of agreement between manual and automated segmentation. In addition, linear regression analysis revealed that the results of texture 2D RBF-based automated segmentation were strongly correlated with the reference manual segmentation, yielding slopes close to 1 and intercepts close to 0 for all the examined morphometric parameters (Figs. 7 to 9).

Indicative results of the different combinations of the proposed methods for one image are shown in Fig. 10, where the superiority of texture-based contour initialization versus the intensity-based one is demonstrated (for example, see the lumen contours in Fig. 10(c) and (d), and compare them with those in (f) and (g), respectively), as well as the superiority of RBF-based contour smoothing versus the LPF-based one (for example, compare the lumen contours in Fig. 10(c) and (d)). In Fig. 11, additional indicative results are shown for the combination of texture-based initialization and RBF-based approximation, that is shown to outperform the other approaches considered in this work. These results demonstrate the suitability of the proposed approach for segmenting heterogeneous IVUS images including images which contain branches, calcified areas and guidewire artifacts.

With respect to the 3D RBF-based contour refinement approach, it is seen from the comparative evaluation results
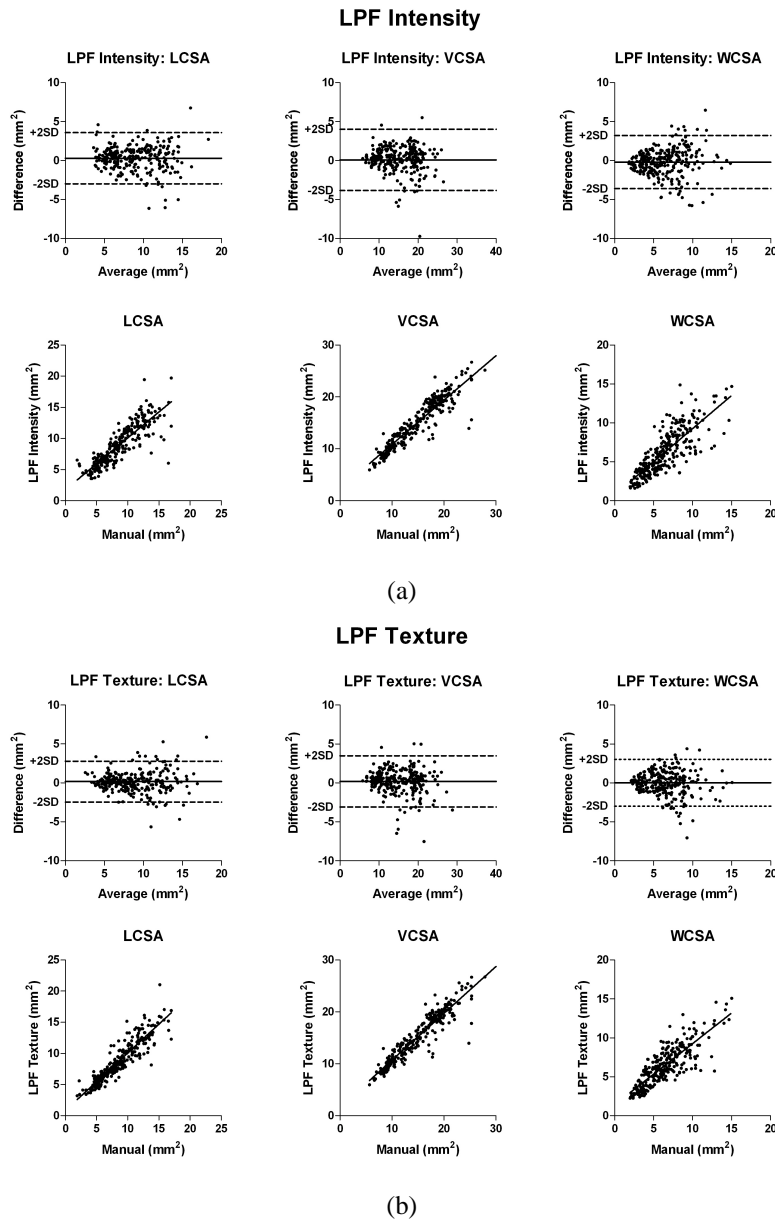
Fig. 7.   Bland-Altman and linear regression plots of the differences between automated and manual segmentation, when (a) intensity-based, (b) texture-based lumen contour initialization, and LPF-based contour refinement are used for the automated contour detection; LCSA: lumen cross-sectional area, VSCA: vessel cross-sectional area, WCSA: wall cross-sectional area.

reported in Table I that this, regardless of the employed initialization procedure, generally results in a higher error than the corresponding 2D approach. This outcome was actually expected and is caused by the fact that, in the absence of any information regarding the correct localization of each IVUS frame in the 3D space, all vessel frames are placed sequentially in a straight line, assuming that this does not deviate significantly from the real three dimensional vessel geometry. This however results in the construction of a straight artery in the 3D space, whose morphology is likely to be quite different than the real one. Under the above restrictive assumption, the information from previous and next frames that is exploited during contour refinement is likely to be incorrect and the effect of this is often seen as a displacement of the detected

boundaries in the 2D plane, as compared to the true ones (Fig. 12). Cardiac motion is another factor contributing to the difficulty in exploiting information available from previous and next frames for the accurate contour refinement in any given frame. The above results justify the choice of performing contour initialization in every IVUS image independently, despite the fact that the proposed initialization processes could easily be modified to take into account the result in the previous frame as well.

Results of statistical analysis of the differences between automated and manual tracings, for the images acquired with the solid-state IVUS system "Volcano", are presented in Table II (Md±SD, i.e. mean and standard deviation of the differences between automated and manual tracings). Indicative results

RBF Intensity
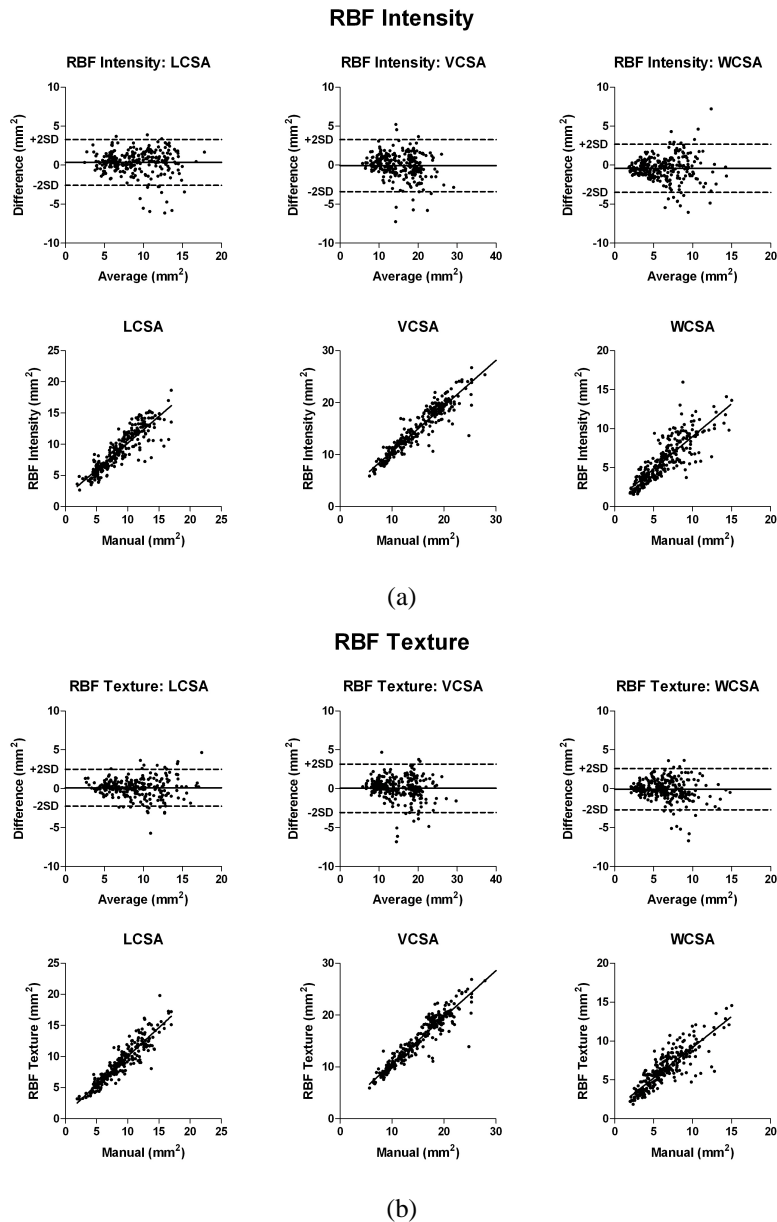

(a)

RBF Texture

(b)

Fig. 8. Bland-Altman and linear regression plots of the differences between automated and manual tracings, when (a) intensity-based, (b) texture-based lumen contour initialization, and 2D RBF-based contour refinement are used for the automated contour detection; LCSA: lumen cross-sectional area, VSCA: vessel cross-sectional area, WCSA: wall cross-sectional area.

of the different combinations of the proposed methods for one image of this set are shown in Fig. 13. These results support the conclusions drawn from the results presented above for the images acquired with the mechanical IVUS system "Boston Scientific", and highlight the possibility of applying the techniques discussed in this work in combination with different image acquisition systems.

Finally, in Table III, the average execution time per frame for the contour initialization and approximation approaches proposed in this work are reported; these were recorded on a 3Ghz PC with 1GB RAM. For initialization, since texture analysis is in any case required for the initialization of the media-adventitia contour, the execution time varies very little with respect to the lumen contour initialization approach that

is followed. As can be seen from Table III, the proposed approaches require relatively limited processing time and consequently their time efficiency is not prohibitive for their use in a clinical environment, after appropriate optimization of the code with respect to computational efficiency.

IV. DISCUSSION

In this paper an automated approach for the detection of lumen and media-adventitia boundaries in IVUS images is presented, based on the results of texture analysis and the use of RBFs. The proposed approach does not require manual initialization of the contours, which is a common requirement of several other prior approaches to IVUS image segmentation. The experiments conducted with the various
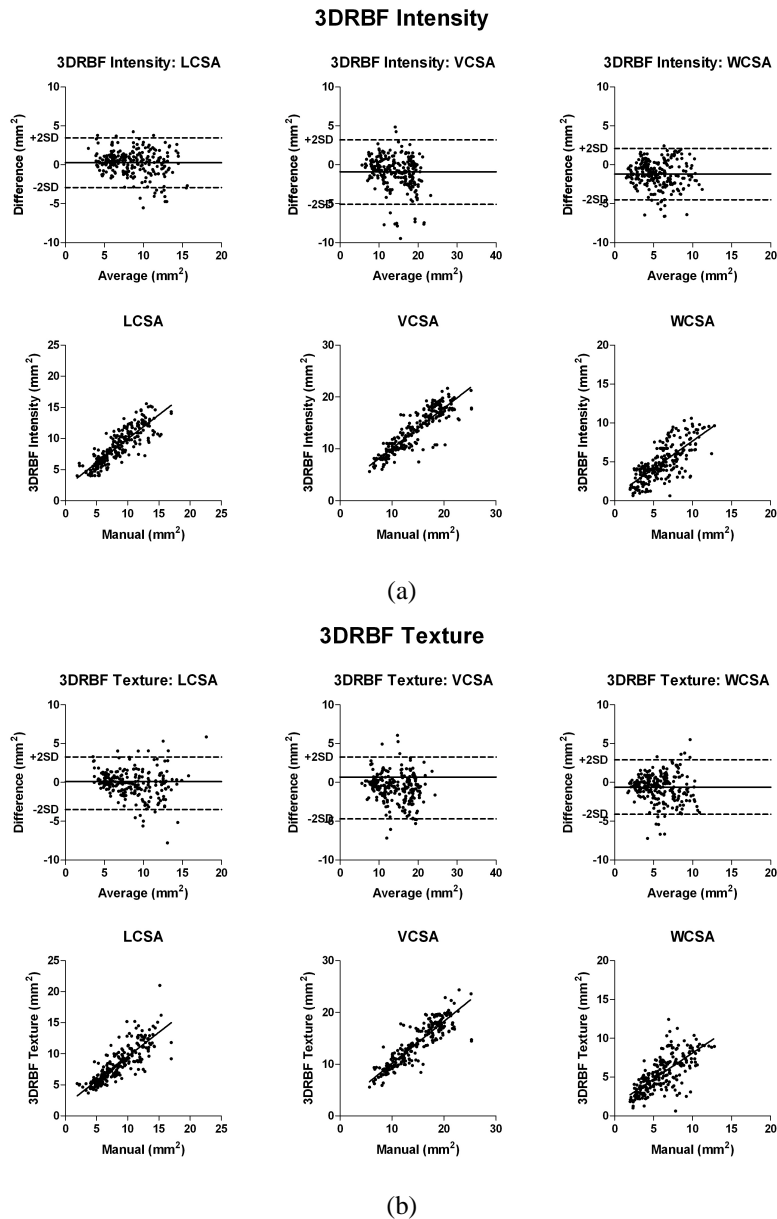
Fig. 9. Bland-Altman and linear regression plots of the differences between automated and manual tracings, when (a) intensity-based, (b) texture-based lumen contour initialization, and 3D RBF-based contour refinement are used for the automated contour detection; LCSA: lumen cross-sectional area, VSCA: vessel cross-sectional area, WCSA: wall cross-sectional area.

combinations of contour initialization and contour refinement methods proposed in this work demonstrated the usefulness of the employed texture features for IVUS image analysis as well as the contribution of the approximation technique based on Radial Basis Functions to the overall analysis outcome. The comparative evaluation of the different examined approaches revealed that use of the texture based initialization and the 2D RBF-based approximation results in a reliable and quick IVUS segmentation, comparable to the manual segmentation.

Our automated segmentation algorithm has several clinical applications. It could facilitate plaque morphometric analysis i.e. planimetric, volumetric and wall thickness calculations, contributing to rapid, and potentially on-site, decision-making. Similarly, our method could be utilized for the evaluation of plaque progression or regression in serial studies investigating the effect of drugs in atherosclerosis. We and others developed and validated an in-vivo IVUS and biplane angiography fusion technique for the geometrically correct 3D reconstruction of human coronary arteries (Giannoglou et al., 2006a), (Slager et al., 2000), (Chatzizisis et al., 2006), (Giannoglou et al., 2006b), (Coskun et al., 2003). This technique is coupled with computational fluid dynamics permitting the investigation of the role of local hemodynamic factors (e.g. endothelial shear stress, tensile stress) (Stone et al., 2003), (Chatzizisis et al., 2007a), (Chatzizisis et al., 2007b), (Chatzizisis et al., 2008) and local geometric parameters (e.g. vessel curvature) (Krams et al., 1997) at certain points along the coronary lumen, on atherosclerosis development and on arterial remodeling.
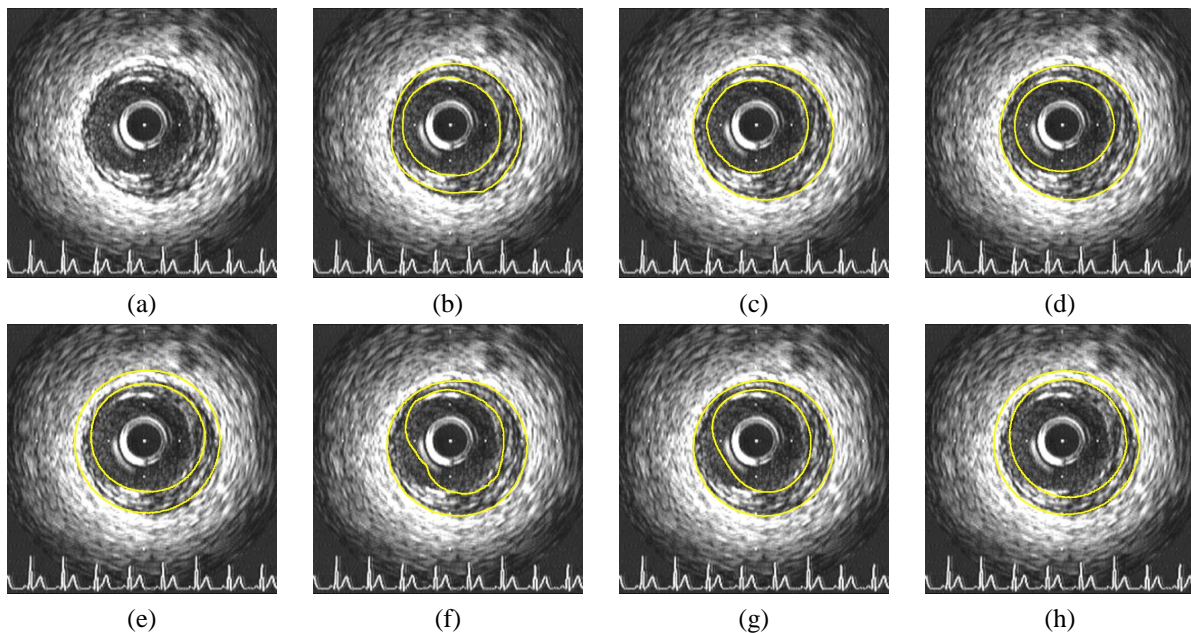
Fig. 10. Experimental results from a representative image acquired with the mechanical IVUS imaging system (a) Original image, (b) Manually segmented image, (c) texture-based initialization, LPF smoothing, (d) texture-based initialization, 2D RBF smoothing, (e) texture-based initialization, 3D RBF smoothing, (f) intensity-based initialization, LPF smoothing, (g) intensity-based initialization, 2D RBF smoothing, (h) intensity-based initialization, 3D RBF smoothing.

TABLE I

MEAN DIFFERENCE BETWEEN AUTOMATIC AND MANUALLY-GENERATED RESULTS AND CORRESPONDING STANDARD DEVIATION FOR THREE IVUS
EVALUATION PARAMETERS, FOR THE IMAGES ACQUIRED WITH THE MECHANICAL IVUS IMAGING SYSTEM.

Parameter/ Method	Lumen area (LCSA) (mm^2)	Vessel area (VCSA) (mm^2)	Wall area (WCSA) (mm^2)
Intensity, LPF	0.298 ± 1.685	0.094 ± 2.01	-0.203 ± 1.75
Texture, LPF	0.169 ± 1.337	0.196 ± 1.679	$\mathbf{0.027} \pm 1.528$
Intensity, 2D RBF	0.362 ± 1.505	-0.063 ± 1.704	-0.425 ± 1.586
Texture, 2D RBF	$0.127 \pm \mathbf{1.209}$	$\mathbf{0.059} \pm \mathbf{1.589}$	$-0.067 \pm \mathbf{1.363}$
Intensity, 3D RBF	0.273 ± 1.619	-0.935 ± 2.112	-1.181 ± 1.681
Texture, 3D RBF	$\mathbf{-0.115} \pm 1.735$	-0.726 ± 2.046	-0.611 ± 1.798

TABLE II

MEAN DIFFERENCE BETWEEN AUTOMATIC AND MANUALLY-GENERATED RESULTS AND CORRESPONDING STANDARD DEVIATION FOR THREE IVUS
EVALUATION PARAMETERS, FOR THE IMAGES ACQUIRED WITH THE SOLID-STATE IVUS IMAGING SYSTEM.

Parameter/ Method	Lumen area (LCSA) (mm^2)	Vessel area (VCSA) (mm^2)	Wall area (WCSA) (mm^2)
Intensity, LPF	0.312 ± 0.552	0.053 ± 0.596	-0.258 ± 0.784
Texture, LPF	0.101 ± 0.381	-0.098 ± 0.577	-0.208 ± 0.695
Intensity, 2D RBF	0.115 ± 0.410	-0.088 ± 0.415	-0.183 ± 0.525
Texture, 2D RBF	$\mathbf{0.092} \pm \mathbf{0.345}$	$\mathbf{-0.047} \pm \mathbf{0.338}$	$\mathbf{-0.140} \pm \mathbf{0.408}$
Intensity, 3D RBF	-0.285 ± 0.551	-0.749 ± 1.190	-0.463 ± 0.895
Texture, 3D RBF	-0.276 ± 0.468	-0.571 ± 1.081	-0.295 ± 0.970

The reliable and quick IVUS segmentation constitutes the foundation for the implementation of the above mentioned reconstruction technique, and the proposed IVUS segmentation method provides this potential.

With respect to the algorithms limitations, it should be noted that the algorithm was not tested with either stents or thrombus in the images. When considering relatively small calcifications, there were no noticeable differences in the algorithm's performance on calcified segments compared to non-calcified segments. When considering larger calcifications, the initialization process for the media-adventitia contour was susceptible to

errors; in several images, however, this was corrected by the subsequent contour approximation process. Regarding the applicability of the proposed approach to images acquired with the use of different catheters and image acquisition systems, our experiments revealed that this is high. However, it may require the experimental re-adjustment of threshold T that is introduced in the lumen contour initialization process. This could possibly be alleviated by further preprocessing of the images, aiming to suppress differences (e.g. in luminance distribution) that may be introduced by the different catheters, due to inter-catheter variability, or the different acquisition

TABLE III

AVERAGE EXECUTION TIMES FOR CONTOUR INITIALIZATION AND APPROXIMATION PROCESSES FOR THE DATASET OF IVUS MAGES ACQUIRED WITH THE MECHANICAL SYSTEM.

Process	Average execution time (per frame)
Contour initialization for both Lumen and Media-Adventitia, using intensity approach for the former	1.81 sec (using C code)
Contour initialization for both Lumen and Media-Adventitia, using texture approach for the former	1.82 sec (using C code)
LPF-based approximation for both Lumen and Media-Adventitia	1.24 sec (using C code)
2D RBF-based approximation for both Lumen and Media-Adventitia	14.09 sec (using Matlab)
3D RBF-based approximation for both Lumen and Media-Adventitia	14.86 sec (using Matlab)
Manual segmentation	85.8 sec

systems.

Future work includes the combination of IVUS image data with a coronary angiography, which will allow the exploitation of information regarding the correct 3D morphology of the vessel, both for the initialization procedure and for the RBF-based contour refinement; the former could also benefit from such an approach, providing that it is extended accordingly. The combined use of texture, intensity and possibly additional information for the initialization step, and the integration of the developed automated analysis methodology to a computer aided diagnosis tool that will also support manual intervention of the medical expert also belong to future work.

V. ACKNOWLEDGEMENTS

REFERENCES

Brusseau, E., de Korte, C., Mastik, F., Schaar, J., van der Steen, A. Fully automatic luminal contour segmentation in intracoronary ultrasound imaging - A statistical approach. IEEE Trans. on Medical Imaging May 2004;23:554–566.

Cardinal, M.-H. R., Meunier, J., Soulez, G., Maurice, R., Therasse, E., Cloutier, G. Intravascular Ultrasound Image Segmentation: A Three-Dimensional Fast-Marching Method Based on Gray Level Distributions. IEEE Trans. on Medical Imaging 2006;25:590–601.

Carr, J., Beatson, R., Cherrie, J., Mitchell, T., Fright, W., McCallum, B., Evans, T. Reconstruction and representation of 3D objects with radial basis functions. In: Proc. of 28th Annual Conference on Computer Graphics and Interactive Techniques August 2001;67–76.

Chatzizisis, Y. Three-dimensional reconstruction of coronary arteries by fusion of intravascular ultrasound and biplane angiography. MSc Dissertation, Aristotle University of Thessaloniki 2004.

Chatzizisis, Y., Giannoglou, G., Matakos, A., Basdekidou, C., Sianos, G., Panagiotou, A., Dimakis, C., Parcharidis, G., Louridas, G. In-vivo accuracy of geometrically correct three-dimensional reconstruction of human coronary arteries: is it influenced by certain parameters? Coronary Artery Dis 2006;17:545–551.

Chatzizisis, Y.S., Jonas, M., Coskun, A.U., Beigel, R., Stone, B.V., Maynard, C., Gerrity, R.G., Daley, W., Rogers, C., Edelman, E.R., Feldman, C.L., Stone, P.H. Prediction of the localization of high-risk coronary atherosclerotic plaques based on low endothelial shear stress: An intravascular ultrasound and histopathology natural history study Circulation 2008, In press.

Chatzizisis, Y.S., Coskun, A.U., Jonas, M., Edelman, E.R., Stone, P.H., Feldman, C.L. Risk stratification of individual coronary lesions using local endothelial shear stress: a new paradigm for managing coronary artery disease Curr Opin Cardiol. 2007;22:552–564.

Chatzizisis, Y.S., Coskun, A.U., Jonas, M., Edelman, E.R., Feldman, C.L., Stone, P.H.Role of endothelial shear stress in the natural history of coronary atherosclerosis and vascular remodeling: molecular, cellular, and vascular behavior J Am Coll Cardiol. 2007;49:2379–2393.

Coskun, A., Yeghiazarians, Y., Kinlay, S., Clark, M., Ilegbusi, O., Wahle, A., Sonka, M., Popma, J., Kuntz, R., Feldman, C., Stone, P. Reproducibility of coronary lumen, plaque, and vessel wall reconstruction and of endothelial shear stress measurements in vivo in humans. Catheter Cardiovasc Interv 2003;60:67–78.

dos S. Filho, E., Yoshizawa, M., Tanaka, A., Saijo, Y., Iwamoto, T. Detection of Luminal Contour Using Fuzzy Clustering and Mathematical Morphology in Intravascular Ultrasound Images. In: Proc. of 27th Annual International Conference of the IEEE Engineering in Medicine and Biology (EMBS), China, September 2005;3471–3474.

dos S. Filho, E., Yoshizawa, M., Tanaka, A., Saijo, Y., Iwamoto, T., Yambe, T., Nitta, S. An adaptive fuzzy segmentation of intravascular ultrasound images. In: IEEE International Symposium on Biomedical Imaging: Macro to Nano April 2004;2:1311–1314.

FarField. FarField Technology, Http://www.farfieldtechnology.com 2001.

Giannoglou, G., Chatzizisis, Y., Koutkias, V., Kompatsiaris, I., Papadogiorgaki, M., Mezaris, V., Parissi, E., Diamantopoulos, P., Strintzis, M. G., Maglaveras, N., Parcharidis, G., Louridas, G. A Novel Active Contour Model for Fully Au-

tomated Segmentation of Intravascular Ultrasound Images: In-Vivo Validation in Human Coronary Arteries. Computers in Biology and Medicine September 2007;37:1292–1302.

Giannoglou, G., Chatzizisis, Y., Sianos, G., Tsikaderis, D., Matakos, A., Koutkias, V., Diamantopoulos, P., Parcharidis, G., Louridas, G. Integration of multi-modality imaging for accurate 3D reconstruction of human coronary arteries in vivo. Nucl Instrum Methods Phys Res A 2006.

Giannoglou, G.D., Chatzizisis, Y.S., Sianos, G, Tsikaderis, D., Matakos, A., Koutkias, V., Diamantopoulos, P., Maglaveras, N., Parcharidis, G.E., Louridas, G.E., In-vivo validation of spatially correct three-dimensional reconstruction of human coronary arteries by integrating intravascular ultrasound and biplane angiography Coron Artery Dis 2006;17:533–543.

Gil, D., Hernandez, A., Rodriguez, O., Mauri, J., Radeva, P. Statistical Strategy for Anisotropic Adventitia Modelling in IVUS. IEEE Trans. on Medical Imaging June 2006;25(6):768–778.

Herrington, D., Johnson, T., Santago, P., Snyder, W. Semi-automated boundary detection for intravascular ultrasound. In: Computers in Cardiology Proceedings. Durham, NC, USA, October 1992;103–106.

Klingensmith, J., Nair, A., Kuban, B., Vince, D. Segmentation of three-dimensional intravascular ultrasound images using spectral analysis and a dual active surface model. In: IEEE International Ultrasonics Symposium September 2004;3:1765–1768.

Klingensmith, J., Shekhar, R., Vince, D. Evaluation of three-dimensional segmentation algorithms for the identification of luminal and medial-adventitial borders in intravascular ultrasound images. In: IEEE Trans. on Medical Imaging 2000;19:996–1011.

Kompatsiaris, I., Tzovaras, D., Koutkias, V., Strintzis, M. Deformable boundary detection of stents in angiographic images. IEEE Trans. on Medical Imaging 2000;19:652–662.

Kovalski, G., Beyar, R., Shofti, R., Azhari, H. Three-dimensional automatic quantitative analysis of intravascular ultrasound image. Ultrasound in Med. and Biol. 2000;26:527–537.

Krams, R., Wentzel, J., Oomen, J., Vinke, R., Schuurbiers, J., de Feyter, P., Serruys, P., Slager, C. Evaluation of endothelial shear stress and 3D geometry as factors determining the development of atherosclerosis and remodeling in human coronary arteries in-vivo: Combining 3D reconstruction from angiography and IVUS (ANGUS) with computational fluid dynamics. Arterioscler. Thromb. Vasc. Biol. 1997;17:2061–2065.

Luo, Z., Wang, Y., Wang, W. Estimating Coronary Artery Lumen Area With Optimization-Based Contour Detection. IEEE Trans. on Medical Imaging April 2003;22(4):564–566.

Mezaris, V., Kompatsiaris, I., Strintzis, M. Still Image Segmentation Tools for Object-based Multimedia Applications. Int. Journal of Pattern Recognition and Artificial Intelligence 2004;18(4):701–725.

Mintz, G., Nissen, S., Anderson, W., Bailey, S., Erbel, R., Fitzgerald, P., Pinto, F., Rosenfield, K., Siegel, R., Tuzcu, E., Yock, P.. American College of Cardiology Clinical Expert Consensus Document on Standards for Acquisition, Measurement and Reporting of Intravascular Ultrasound Studies (IVUS). A report of the American College of Cardiology Task Force on Clinical Expert Consensus Documents. Journal of the American College of Cardiology 2001;37:1478–1492.

Papadogiorgaki, M., Mezaris, V., Chatzizisis, Y., Kompatsiaris, I., Giannoglou, G. A Fully Automated Texture-based Approach for the Segmentation of Sequential IVUS Images. In: Proc. 13th Int. Conference on Systems, Signals and Image Processing (IWSSIP), Hungary, September 2006;461–464.

Parissi, E., Kompatsiaris, Y., Chatzizisis, Y., Koutkias, V., Maglaveras, N., Strintzis, M., Giannoglou, G. An Automated Model for Rapid and Reliable Segmentation of Intravascular Ultrasound Images. In: Proc. of the 7th International Symposium on Biological and Medical Data Analysis (ISBMDA'06), Thessaloniki, Greece, December 2006.

Perrey, C., Scheipers, U., Bojara, W., Lindstaedt, M., Holt, S., Ermert, H. Computerized segmentation of blood and luminal borders in intravascular ultrasound. In: Proc. of the 2004 IEEE Ultrasonics Symposium August 2004;2:1122–1125.

Plissiti, M., Fotiadis, D., Michalis, L., Bozios, G. An Automated Method for Lumen and Media-Adventitia Border Detection in a Sequence of IVUS Frames. IEEE Trans. on Information Tech. in Biomedicine June 2004;8(2).

Slager, C., Wentzel, J., Schuurbiers, J., Oomen, J., Kloet, J., Krams, R., von Birgelen, C., van der Giessen, W., Serruys, P., de Feyter, P. True 3-dimensional reconstruction of coronary arteries in patients by fusion of angiography and IVUS (ANGUS) and its quantitative validation. Circulation 2000;102:511–516.

Sonka, M., Zhang, X., Siebes, M., Bissing, M., DeJong, S., Collins, S., McKay, C. Segmentation of intravascular ultrasound images: A knowledge-based approach. IEEE Trans. on Medical Imaging 1995;14:719–732.

Stone, P., Coskun, A., Kinlay, S., Clark, M., Sonka, M., Wahle, A., Ilgebusi, O., Yeghiazarians, Y., Popma, J., Orav, J., Kuntz, R., Feldman, C. Effect of endothelial shear stress on the progression of coronary artery disease, vascular remodeling and in-stent restenosis in humans. Circulation 2003;108:438–444.

Unal, G., Bucher, S., Carlier, S., Slabaugh, G., Fang, T., Tanaka, K. Shape-driven Segmentation of Intravascular Ultrasound Images. In: Proc. of First International Workshop on Computer Vision for Intravascular and Intracardiac Imaging (CVII 2006) at MICCAI 2006, Copenhagen, Denmark, October 2006;51–58.

Unser, M. Texture classification and segmentation using wavelet frames. IEEE Trans. on Image Processing, November 1995;4(11):1549–1560.

Zhu, H., Liang, Y., Friedman, M. IVUS image segmentation based on contrast. In: Proc. of SPIE, Durham, NC, USA, 2002;4684:1727–1733.
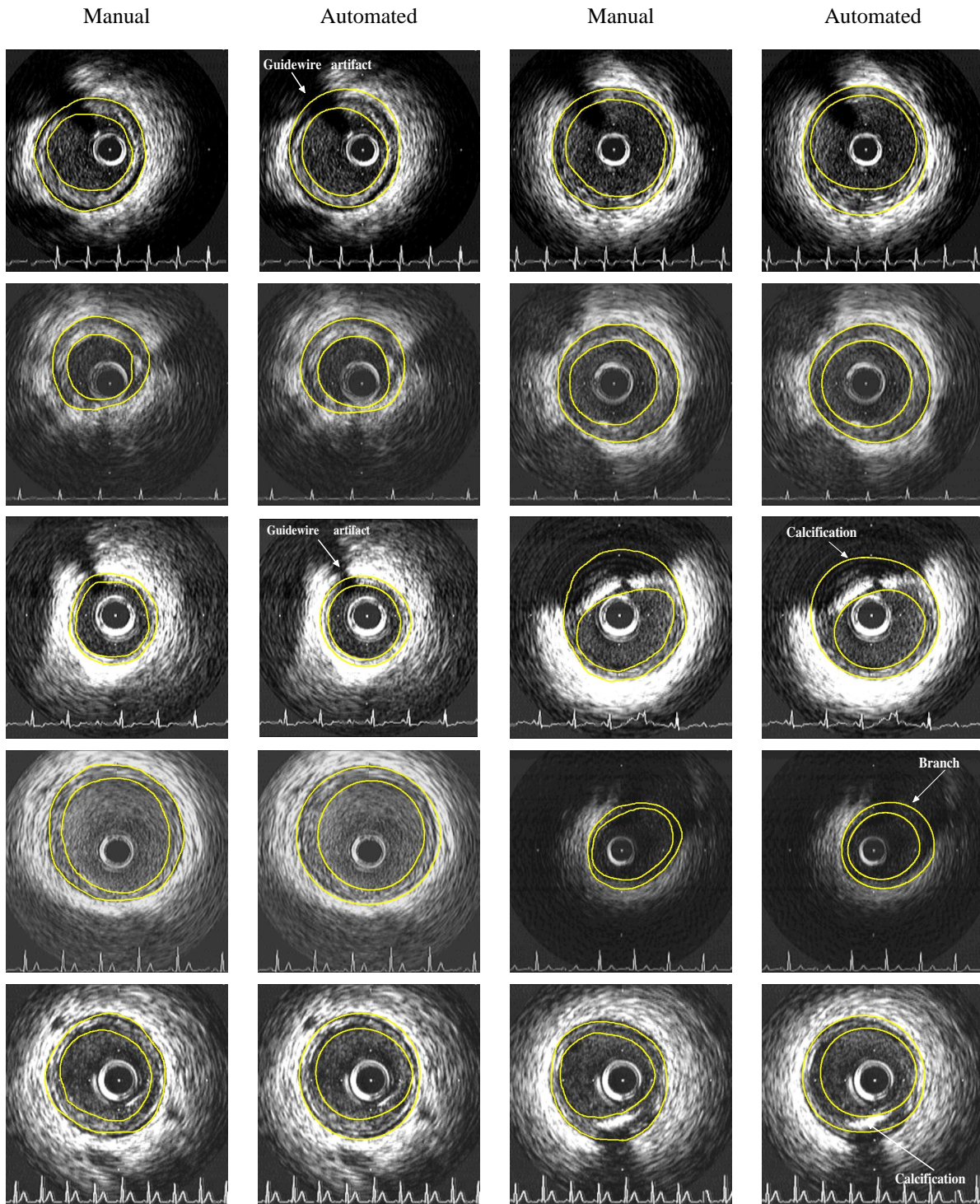
Fig. 11. Experimental results for different images of the proposed approach using texture-based contour initialization and RBF-based approximation, shown on the second and fourth column, and comparison with corresponding contours manually generated by medical experts on the first and third column accordingly.
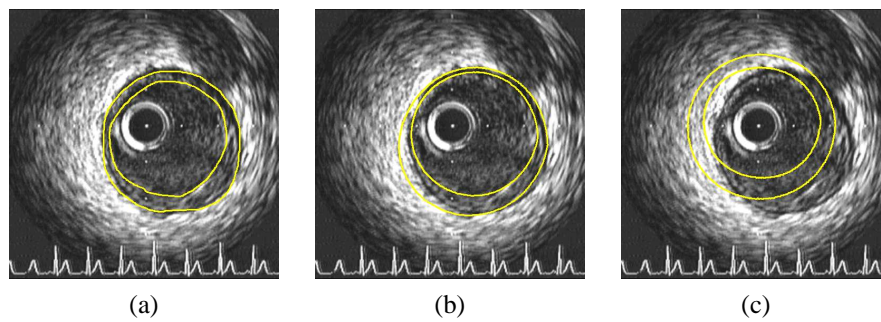
Fig. 12.   (a) Original IVUS image manually segmented, (b) segmentation by texture-based contour initialization and 2D RBF-based refinement, (c) segmentation by texture-based contour initialization and 3D RBF-based refinement. The displacement of the contours, due to failure of the simple assumptions made for the 3D geometry of the vessel, is evident in (c).
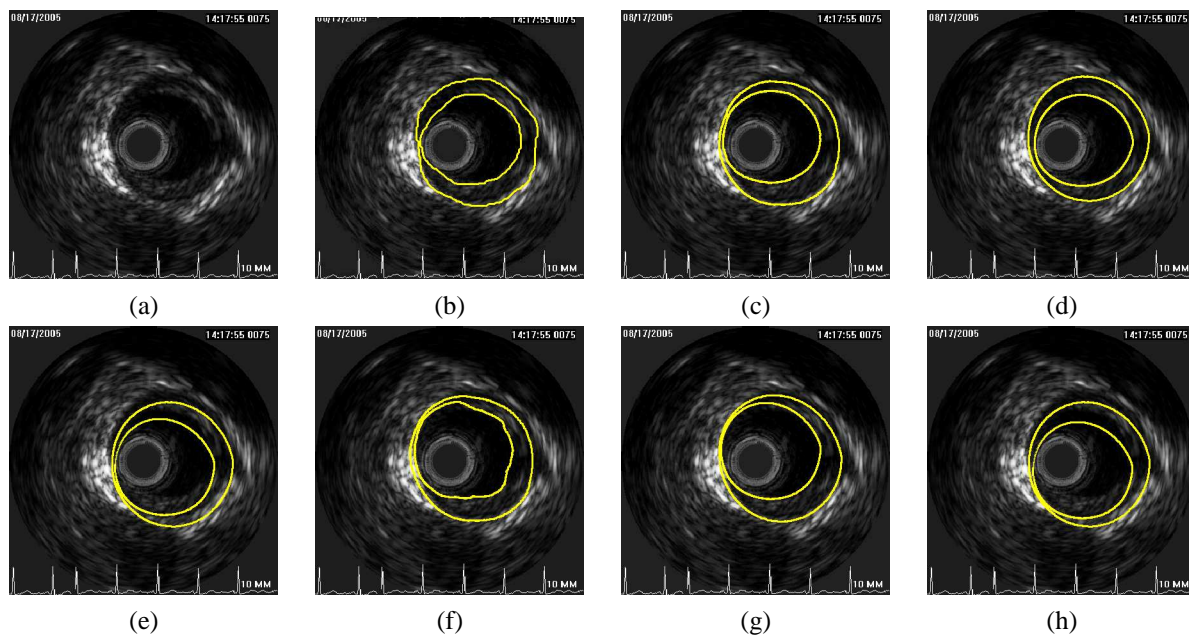

Fig. 13.   Experimental results acquired with the solid-state IVUS imaging system. (a) Original image, (b) Manually segmented image, (c) texture-based initialization, LPF smoothing, (d) texture-based initialization, 2D RBF smoothing, (e) texture-based initialization, 3D RBF smoothing, (f) intensity-based initialization, LPF smoothing, (g) intensity-based initialization, 2D RBF smoothing, (h) intensity-based initialization, 3D RBF smoothing.